



# Dynamic Behavior of AA2519-T8 Aluminum Alloy Under High Strain Rate Loading in Compression

A. T. Olasumboye<sup>1</sup> · G. M. Owolabi<sup>1</sup> · A. G. Odeshi<sup>2</sup> · N. Yilmaz<sup>1</sup> · A. Zeytinci<sup>3</sup>

Received: 7 June 2017 / Accepted: 24 January 2018 / Published online: 6 February 2018  
© Society for Experimental Mechanics, Inc 2018

## Abstract

In this study, the effects of strain rate on the dynamic behavior, microstructure evolution and hence, failure of the AA2519-T8 aluminum alloy were investigated under compression at strain rates ranging from 1000 to 3500 s<sup>-1</sup>. Cylindrical specimens of dimensions 3.3 mm × 3.3 mm (L/D = 1) were tested using the split-Hopkinson pressure bar integrated with a digital image correlation system. The microstructure of the alloy was assessed using optical and scanning electron microscopes. Results showed that the dynamic yield strength of the alloy is strain rate dependent, with the maximum yield strength attained by the material being 500 MPa. The peak flow stress of 562 MPa was attained by the material at 3500 s<sup>-1</sup>. The alloy also showed a significant rate of strain hardening that is typical of other Al–Cu alloys; the rate of strain hardening, however, decreased with increase in strain rate. It was determined that the strain rate sensitivity coefficient of the alloy within the range of high strain rates used in this study is approximately 0.05 at 0.12 plastic strain; a more significant value than what was reported in literature under quasi-static loading. Micrographs obtained showed potential sites for the evolution of adiabatic shear band at 3500 s<sup>-1</sup>, with a characteristic circular-shaped surface profile comprising partially dissolved second phase particles in the continuous phase across the incident plane of the deformed specimen. The regions surrounding the site showed little or no change in the size of particles. However, the constituent coarse particles were observed as agglomerations of fractured pieces, thus having a shape factor different from those contained in the as-received alloy. Since the investigated alloy is a choice material for military application where it can be exposed to massive deformation at high strain rates, this study provides information on its microstructural and mechanical responses to such extreme loading condition.

**Keywords** Aluminum alloy · High strain rate · Dynamic response · Strain localization · Adiabatic shear bands

## Introduction

Aluminum alloys are reputed for their high strength-to-weight ratio, high specific stiffness and low density, which favor their use in wing skins and fuselage structure of commercial and military aircraft [1]. A few other desirable properties of aluminum alloys include good corrosion resistance, excellent machinability, high thermal conductivity, high electrical conductivity and high ductility. The AA2000

series are precipitation-hardenable aluminum alloys with copper as the principal alloying element [2]. Compositional control and advanced processing of the aluminum–copper alloy system have led to improved properties for various applications. For instance, Al<sub>2</sub>CuMg intermetallic compounds form as second phase particles to further improve the strength and the enhance fracture toughness of the alloy [1, 3]. Consequently, Al–Cu–Mg alloys find widespread applications in aircraft and automobile structures, where the combination of weight reduction and strength improvement are both sought in order to minimize operational costs without compromising performance [4]. It has been established that AA2519 armor grade alloy, when tempered to certain specified conditions, possesses excellent ballistic protection characteristics equivalent to those of AA7039 and is less susceptible to stress corrosion cracking when compared to AA5083 [5]. Being easily weldable with filler alloy AA2319, its yield strength as welded butt joints is

✉ A. T. Olasumboye  
adewaleola1@yahoo.com

<sup>1</sup> Department of Mechanical Engineering, Howard University, Washington, DC 20059, USA

<sup>2</sup> Department of Mechanical Engineering, University of Saskatchewan, Saskatoon, Canada

<sup>3</sup> Department of Civil Engineering, University of District Columbia, Washington, DC 20008, USA

higher than the yield strengths of other commercially available alloys [5]. Other selling points of AA2519 alloy, such as its age-hardenability and heat-treatability in the post-weld condition make it an alloy of choice because these features allow for the improvement of its mechanical properties when compared to the as-welded condition [6]. Another emerging application for AA2519 alloy is superplastic forming [7]. Superplasticity of metals is an important property in the fabrication of complex parts from sheet metals.

The growing number of applications of aluminum alloys in both aerospace and automotive industries has necessitated a better understanding of the material behavior from the quasi-static regime to the high rate regime. Combination of these evolving applications and the constantly renewed interest in the plastic behavior of aluminum alloys under dynamic impact or shock loading conditions, which can be on the order of  $10^3 \text{ s}^{-1}$  constitute a major impetus for further understanding of their failure mechanisms at such high strain rates [8]. Other sources of motivation are the issues of safety and reliability of defense and aerospace structures most especially with increasing incidence of bird strikes which constitute a major air-flight danger in the world and ballistic impact on military vehicles during combat operations. Therefore, understanding the property changes associated with high strain rate loading during the material deformation is an important step in the characterization of the dynamic behavior of the alloys. This, in turn, provides useful information which facilitates improved material design and proper selection for high-performance service requirements.

During high strain-rate loading, a work-hardening region of the deformation profile is followed by flow stress, which is contingent upon a complex combination of contributions from relevant strengthening contributors which may include dislocation interactions, solute hardening, and hardening by dispersoids and second phases among others [9, 10]. Plasticity and work-hardening of Face Centered Cubic materials have been explained by the concepts of dislocations [11]. The investigated material is a precipitation hardened aluminum alloy. Precipitation hardening relies on strengthening by fine precipitates which form during heat treatment and very effective in impeding the motion of dislocations. The result of this immobilization of dislocation is responsible for strengthening or hardening.

The deformation and failure of metallic alloys under quasi-static loading are generally by slip and twinning while a failure at high strain rate is initiated by intense localization of shear strain. When metallic alloys are subjected to such extreme loading conditions, phenomena such as phase

transformation, twinning, void formation, dynamic recovery or dynamic recrystallization can occur the kinetics of each of which are different [12]. Bai et al. [13] reported that during large plastic deformations, about 90% of the applied deformation energy is converted into heat, causing a rise in temperature in the deforming material. This may ultimately lead to localized plastic flow due to adiabatic heating. However, part of the mechanical energy for plastic deformation is stored in the material microstructure as internal residual energy [14]. In reality, the quantity of heat dissipation from plastic work depends on the thermal diffusivity of the material, strain, local strain rate and temperature [13, 14]. The undesirable effect of localized heating is intense localized shearing and fracture. The evolution of adiabatic shear band (ASB) begins with the formation of deformed ASBs (also called deformed bands) characterized by highly deformed and elongated grains. The literature is replete with information on the microstructural evolution during high strain-rate loading and other events leading to shear fracture of various aluminum alloys and other metallic materials, while high strain-rate studies on AA2519 are limited [15–17]. Hence, it is imperative to understand the microstructural response of AA2519-T8 aluminum alloy when subjected to high-rate compression loading. This is the focus of the current study.

The objectives of this paper were to investigate the high strain-rate deformation of aluminum alloy AA2519-T8, employed in the design of lightweight armored military equipment, and define its microstructural evolution during its dynamic deformation at high strain rates. The intent is to provide its material properties database that can be used to validate current or future constitutive models for predicting its dynamic response under high strain rate compressive loading. These experimental data include significant information on the dynamic yield and flow stresses, the strain rate sensitivity (SRS) and microstructural evolution of the material and can be used in the formulation and validation of robust constitutive models for simulating the material's response at high strain rates.

## Materials and Methods

The investigated AA2519 (AlCu6Mn) alloy was received in T8 temper condition. The alloy contains 5.3–6.5% copper and other trace elements as shown in Table 1. The as-received plates were machined to cylindrical test specimens having 3.3 mm in diameter and 3.3 mm long (aspect ratio,  $L/D = 1$ ). Split-Hopkinson pressure bar (SHPB) and digital

**Table 1** Elemental composition of AA2519 aluminum alloy

Composition	Al	Cu	Fe	Mg	Mn	Si	Ti	V	Zn	Zr
Wt%	91.5–93.8	5.3–6.4	0.3	0.05–0.4	0.1–0.5	0.25	0.02–0.1	0.05–0.15	0.1	0.1–0.25

image correlation (DIC) systems were used concurrently for capturing the compression data from the test specimens during the mechanical loading. The photograph of the SHPB used for mechanical testing is shown in Fig. 1. It comprises the incident and the transmitter bars which are made of Ti-6Al-4V alloy, each 13 mm in diameter and 1905 mm in length. Strain gages were bonded to each of the bars at equidistance of 947 mm from the test specimen. At both locations, the strain gages were connected to a full Wheatstone bridge circuit which was configured to capture the axial loads as elastic waves. The elastic wave data captured as voltage–time signals by the strain gages on the incident and the transmitter bars were converted to their corresponding load values using a conversion factor obtained from an initial calibration of the equipment. The elastic waves are longitudinal for compressive loading and comprise the incident, the reflected and the transmitted waves. A schematic representation of the wave propagation towards and away from the specimen is inserted in Fig. 1. The amount of wave reflected by the specimen is a function of the material properties.

Based on one-dimensional wave theory and on the assumption that the forces acting on both ends of the test specimen are equal, the mean values of force, true stress, true strain and strain rate in the specimen were determined

mathematically using appropriate equations that are well described in the literature [8, 18]. Also, SRS plot was generated using the following relation [19]:

$$m = \frac{\partial \ln \sigma(\dot{\epsilon})}{\partial \ln \dot{\epsilon}}, \quad (1)$$

where  $m$  is the SRS,  $\sigma(\dot{\epsilon})$  is the flow stress in MPa at fixed plastic strain, and  $\dot{\epsilon}$  is the strain rate in  $\text{s}^{-1}$ .

Prior to putting the test specimen between the bars, the contacting surfaces of the bars and those of the specimen were cleaned using acetone and M-prep neutralizers. The contact surfaces between the bars and test specimens were subsequently lubricated with a thin film of molybdenum disulphide ( $\text{MoS}_2$ ) in order to reduce the effect of friction and prevent any shear traction on the specimens' surfaces during deformation. A stopper piston built at the right end of the transmitter bar was designed for safe collection and containment of the transmitter bar at the end of the impact in order to prevent any secondary loading during the experiment (i.e., for momentum trapping). The piston is stuffed with Play Doh™ (Hasbro, USA), a pliable dough-like material before the test. The dough material absorbs the kinetic energy of the transmitted bar, thereby bringing it to a smooth and safe halt after the impact.

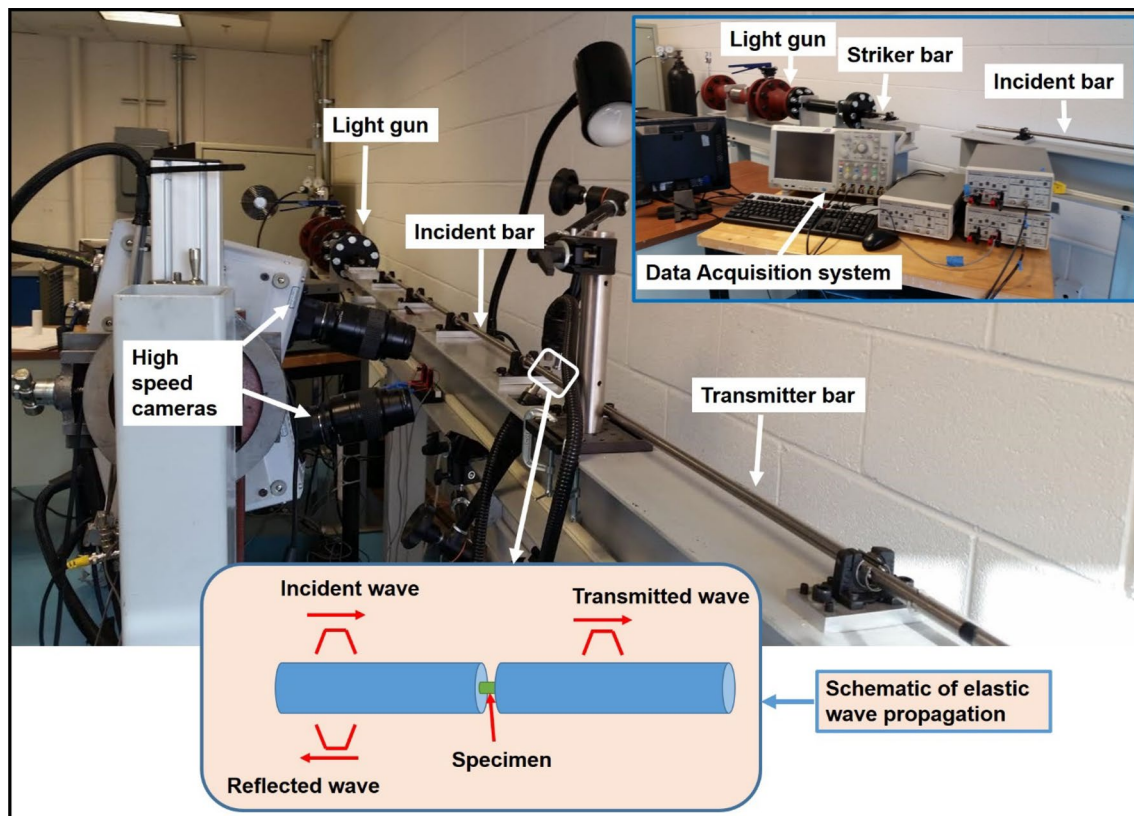


**Fig. 1** Experimental set-up showing SHPB synchronized with high speed cameras for in-situ strain measurement using digital image correlation technique

The experiment was run three times, and an average of the three strain rate data obtained was taken and reported to the nearest hundred. Averaging out the data obtained for the three runs at each strain rate also made the strain rate vs. true strain plot fairly constant. Typical plots of the stress vs. strain (for one and two wave stress) and strain-rate vs. strain plots obtained for the alloy impacted at an average strain rate of  $3000\text{ s}^{-1}$  are presented in Fig. 2a to demonstrate the validity of the test results. At the corresponding pressures, the specimens were tested at approximate strain rates of 1000, 1500, 2000, 2500, 3000 and  $3500\text{ s}^{-1}$ . Figure 2b, c show the typical voltage vs. time (V–T) signal and those obtained for multiple experiments respectively, at an average strain rate of  $3000\text{ s}^{-1}$ .

In situ strain data acquisition was accomplished using the DIC system. The system, synchronized with the SHPB apparatus, is comprised of two high speed Photron Fast-Cam™ SA5 cameras which were set at angles of  $45^\circ$  and  $-45^\circ$  to the horizontal, while focusing on the horizontally positioned specimen. The cameras have a maximum frame rate of 1,000,000 frames per second (fps) and a maximum

resolution of  $64\text{ pixels} \times 16\text{ pixels}$  at  $1/(2,712,000)$  second shutter speed. Photron software was used for activating the cameras at select trigger modes during the testing. The picture frames obtained in this study were captured at the frame rate of 124,000 fps and  $64 \times 16$  pixels resolution. A total of 131,000 images were taken for each experiment. In order to prepare the specimen for both the SHPB experiment and the DIC testing technique simultaneously, a speckled pattern of black and white dots was applied to its circumferential area by painting the specimens. The evolution of strain along the specimen was captured in the series of images produced as the specimens deformed under compressive high strain rate loading. Aramis™ software, developed by Trillion Quality Inc., was used to obtain the strains along the deformed specimens.

The post-impact metallographic specimen preparation for microstructural characterization, involved surface grinding and polishing using  $9\text{ }\mu\text{m}$  Struer's MD Largo™ disc and emery cloths (ranging from 3 to  $0.02\text{ }\mu\text{m}$ ) respectively, with the recommended solutions. The polished surfaces (compression plane) of the test specimens were etched using a

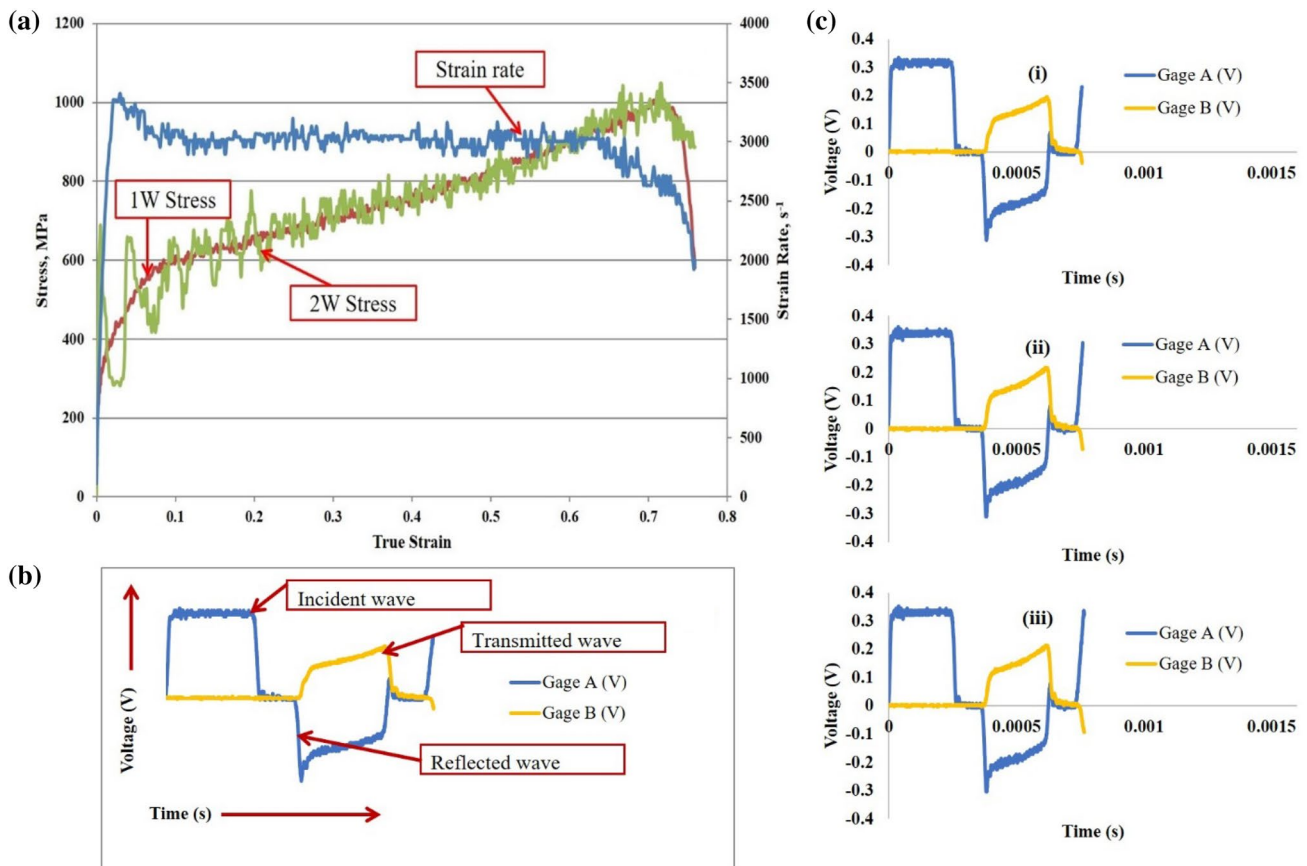


**Fig. 2** Plots showing **a** stress–strain response of AA2519-T8 aluminum specimen including one- and two-wave stress curves and the strain rate, **b** typical V–T signal of the compression experiment com-

prising incident, reflected and transmitted waves, and **c** multiple V–T signals, at an average strain rate of  $3000\text{ s}^{-1}$

solution consisting of 25 ml methanol, 25 ml HCl, 5 ml HNO<sub>3</sub> and a drop of HF. The etching time ranged between 30 and 40 s, depending on the severity of the compression load. The etched specimens were rinsed thoroughly using methanol and air-dried. Microstructures of the specimens were then evaluated using optical microscopy (OM) and scanning electron microscopy (SEM). The OM used is a Nikon ECLIPSE MA200. Its imaging analysis software is NIS Elements version 4.20. The SEM used is a JEOL JSM-7600F, and secondary electron imaging at an accelerated voltage of 20 kV was used.

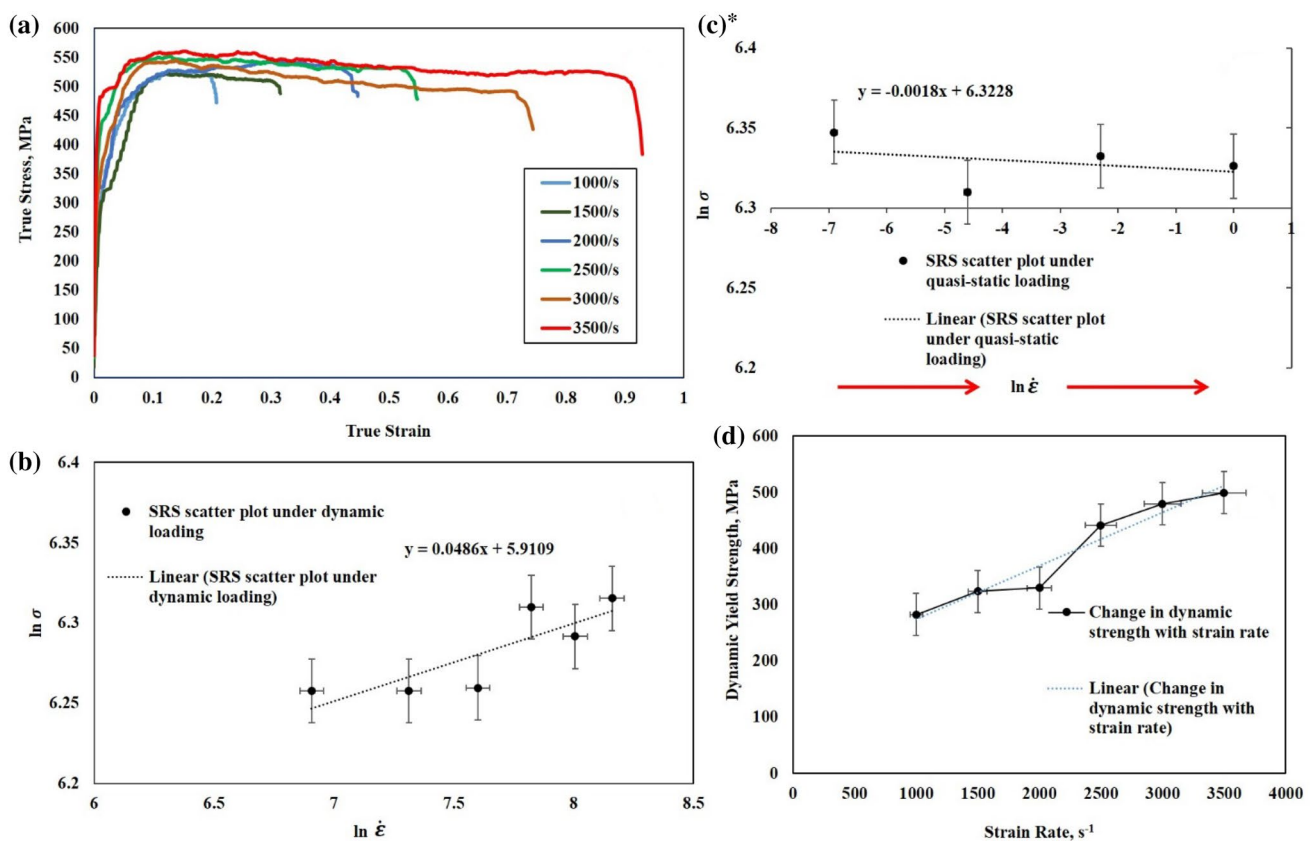
## Results and Discussion

### Dynamic Mechanical Response

The true stress–true strain curves for the AA2519-T8 aluminum alloy obtained at six different strain rates are presented in Fig. 3a. Figure 3b shows a plot of log of stress vs. log of strain rate, which provides the SRS of the alloy at 0.12

plastic strain under high strain rates. Figure 3c was obtained from the quasi-static compressive test results in Macar [20], in the range of strain rates  $10^{-3}$ – $10^0$  s<sup>-1</sup>, in order to provide information on the SRS of the same alloy under quasi-static loading. The variation of its yield strength with strain rate is provided in Fig. 3d. It is observed in Fig. 3a that all the true stress–true strain curves have distinct points of yield except that which was obtained at the lowest strain rate of 1000 s<sup>-1</sup>. At 1000 s<sup>-1</sup>, the curve shows both regions of elastic and plastic deformation without a clear yield point. At higher strain rates, the yield points are clearly identified with an initial slight drop in flow stress at yield point. Beyond the yield point, there is a decline in the rate of stress increase and the plastic portion is characterized by strain hardening to the maximum strain of 0.20. Strain hardening is a consequence of dislocation multiplications as the materials deformed plastically. The effects of dislocation mobility, density or patterning on the strength of metallic alloys have been extensively studied [11].

Peak flow stresses of 528, 523 and 542 MPa were observed at strain rates of 1000, 1500 and 2000 s<sup>-1</sup>,



\* Referenced work from [20]

**Fig. 3** Results showing **a** dynamic true stress–true strain curves, **b** strain rate sensitivity at 0.12 plastic strain under dynamic loading, **c** strain rate sensitivity at 0.12 plastic strain under quasi-static loading

[20], and **d** yield strength variation with strain rate for the investigated AA2519-T8 alloy under impact loads

respectively. These values agree with the average ultimate tensile strength of about 550 MPa reported in Macar [20]. Moreover, in Macar [20], it was reported that the peak flow stress is nearly the same for the range of quasi-static strain rates used (i.e.,  $0.001\text{--}1\text{ s}^{-1}$ ) indicating that the material is not strain rate sensitive in the quasi-static regime. When deformed at high strain rates of 2500, 3000 and  $3500\text{ s}^{-1}$ , the peak flow stress values attained by the material were determined to be 552, 545, 560 MPa, respectively. The true stress–true strain curves of the material at 3000 and  $3500\text{ s}^{-1}$  were observed to plateau at corresponding peak flow stress values as strain-hardening slowed down to give way for a marginal but steady decline in flow stress over a range of strains depending on strain rate, due to thermomechanical instabilities. This behavior is attributable to thermal softening. Thermal softening is a phenomenon which results from an increase in temperature as a result of the conversion of deformation energy to thermal energy. Although the total strain attained by the material that was deformed at  $3500\text{ s}^{-1}$  strain rate is about 0.90, the rate of flow softening remains marginal. The macroscopic inspection of the tested specimen did not reveal any fracture, while further testing at a strain rate higher than  $3500\text{ s}^{-1}$  is limited by specimen size constraint. Therefore, the total strain to failure is expected to be more than 0.90. This is an indication of high ductility that is typical of the AA2519 aluminum alloy. This property behavior has been found in a study [7] to be significant at high temperatures ranging from 450 to 535 °C. In the study, Zuiko et al. investigated the superplasticity of a thermo-mechanically processed AA2519 alloy and determined the highest elongation-to-failure of ~750% at a temperature of 525 °C. The alloy shows significant rates of strain hardening from low to high strain rates, thus exhibiting high strength. It has been reported that AA2519 has 20% higher yield strength than AA2219 (another Al–Cu alloy) in the same T8 temper condition [21]. It was however reported that the rate of strain hardening decreased with increasing strain rate.

In Fig. 3b, c, the SRS values of the alloy at 0.12 plastic strain in the dynamic high strain rate and quasi-static loading regimes respectively, were determined as shown in the figures. The linear fit (based on the least squares method) of the logarithm of the true stress vs. the logarithm of the strain rate plots for the high-rate loading of the material indicates the SRS ( $m$ ) to be approximately 0.05 while the value is  $-0.0018$  under quasi-static loading. Fitting was done because it appears that at higher strain rates, the rate controlling mechanisms are changing perhaps due to thermomechanical instabilities of the material at those rates. The lower value of  $m$  and near-constant SRS plot observed based on the quasi-static data reported by Macar [20] for the material (Fig. 3c) may be an indication of the insensitivity of the material to strain rate in the quasi-static loading regime. The negative-valued  $m$  may also be of no consequence, since

the difference in the logarithmic values of flow stress in Fig. 3c appears statistically insignificant, but could have an impact on the line fit. In Macar [20], the material was mainly considered as insensitive to strain rate under quasi-static loading at room temperature notwithstanding the negative SRS, which is often an indication of dynamic strain aging, because there was no evidence of serrated flow in the material. Cadoni et al. [22] also reported strain rate insensitivity for AA2519 with similar heat treatment at different plastic strains with no experimental evidence of serrated flow for the material tested under quasi-static loading at room temperature. A higher value of  $m$  indicates higher ductility while materials with  $m > 0.33$  exhibit superplasticity [7]. It has been reported for superplastic flow that the value of SRS is related to strain rate  $\dot{\epsilon}$  such that the maximum value of the SRS corresponds to the optimum strain rate [23]. The parameter depends on other factors including strain, average grain size, and temperature of deformation [23, 24]. Regardless of the technical route adopted for grain refinement, FCC metals showed an increase in SRS values with grain size reduction [25]. Grain refinement of the AA2519 alloy by thermo-mechanical processing was reported to improve its SRS significantly when subjected to high-temperature superplastic testing [7]. Armstrong and Walley [24], in their review of high strain rate properties of metals and alloys, reported that SRS was only noticeable in the strain hardening behavior of FCC metals such as copper and aluminum, while it was observed to be significant only in the yield stress of BCC metals and alloys like steel. However, in Fig. 3d, it is shown that the yield strength of AA2519-T8 alloy exhibited a notable strain rate dependency from 283 MPa at  $1000\text{ s}^{-1}$  to 500 MPa at  $3500\text{ s}^{-1}$ . The quasi-static yield strength values reported for this material by Macar [20] and Thom [26] in their experimental studies are about 420 and 421, respectively. These values fall within the range of dynamic yield strengths ( $283\text{ MPa} \leq \sigma_y \leq 500\text{ MPa}$ ) obtained for the material within the range of high strain rates examined in this study. Moreover, in Macar [20], it was reported that the yield strength of the material is almost the same for all the strain rates used for the quasi-static tests (i.e., 0.001, 0.01, 0.1 and  $1\text{ s}^{-1}$ ) at room temperature. This is expected since most AA2000 aluminum alloys that are strain rate insensitive under quasi-static load at room temperature. However, for the high strain rate regime studied in this work, Fig. 3d shows that the rate of the dynamic yield strength increase between 1000 and  $2500\text{ s}^{-1}$  is higher than the rate of increase between 2500 and  $3500\text{ s}^{-1}$ . The SRS value obtained in this study is consistent with those that other researchers have reported for aluminum in the literature [25].

The DIC system images of the compressed specimen, taken at 0, 48, 96, 144 and 192  $\mu\text{s}$  in the deformation history for specimen deformed at  $3000\text{ s}^{-1}$  are shown in Fig. 4, to demonstrate the initiation, propagation, and localization of

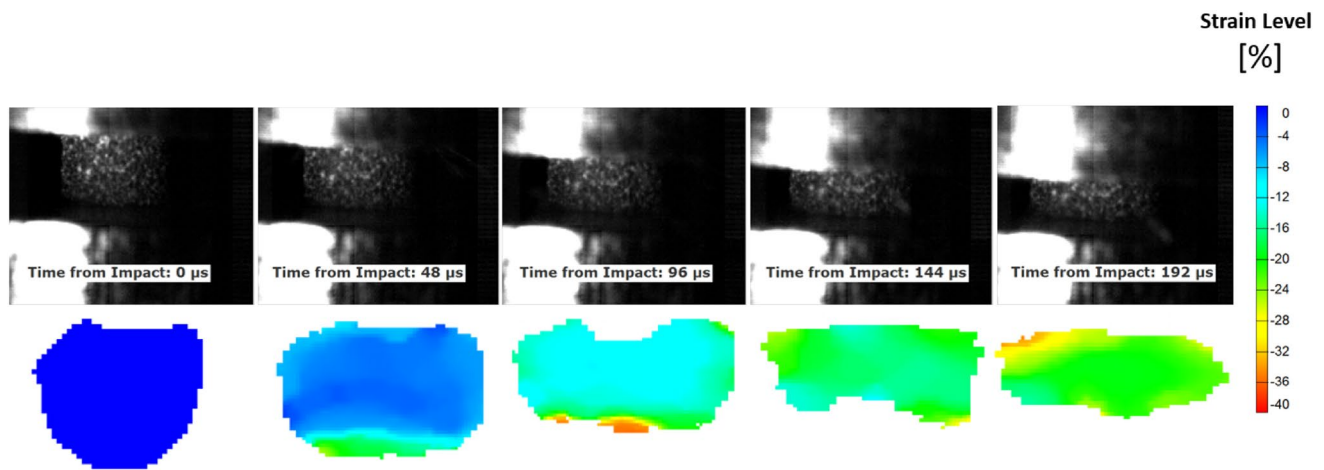


**Fig. 4** DIC images of the deformed specimen at different stages of compression with corresponding strain map, showing the progression of strain localization along the specimen at  $3000 \text{ s}^{-1}$

surface plastic strain along the specimen. The scale legend in the right corner of the figure ranks strain level from zero to  $-40\%$ , with a color other than blue indicating increase in strain level. Blue and red colors are the two extremes with 0 and  $-40\%$  values respectively. Negative strain denotes compression as opposed to axial tension in which strain is positive. It is observed that the strain level at the beginning of the test is zero while at  $48 \mu\text{s}$ , strain has developed to about  $20\%$  from the transmitter-bar end of the specimen. At the base of the specimen, the strain has built up to a significant value around the maximum at time  $t = 96 \mu\text{s}$  and was observed to have propagated and distributed along the specimen at  $144 \mu\text{s}$ . At  $192 \mu\text{s}$ , higher strains are observed to have localized along an apparent plastic flow path within the specimen and on the incident-bar end of the specimen. It can, therefore, be inferred that plastic strain develops, propagates and gets localized from the transmitter-bar end to the incident-bar end of the sandwiched specimen in the SHPB compression test. This strain localization direction explains the reason why the incident surface of the shear compression specimen is often prepared for microstructural investigation.

### Microstructure of the As-Received Alloy

Figures 5 and 6 show the results of the microstructural investigation of the as-received alloy using OM and SEM, respectively. From the micrographs in Fig. 5, dispersed second phase particles were identified within a continuous phase of  $\alpha$ -aluminum. Some of the particles are seen to be aligned along the rolling direction of the alloy. Based on size difference, the second-phase particles can be categorized into coarse and fine-sized particles. The two categories exhibit irregular shape but different sizes. The equivalent dimension of the coarse particles ranges from 22 to  $90 \mu\text{m}$ . SEM

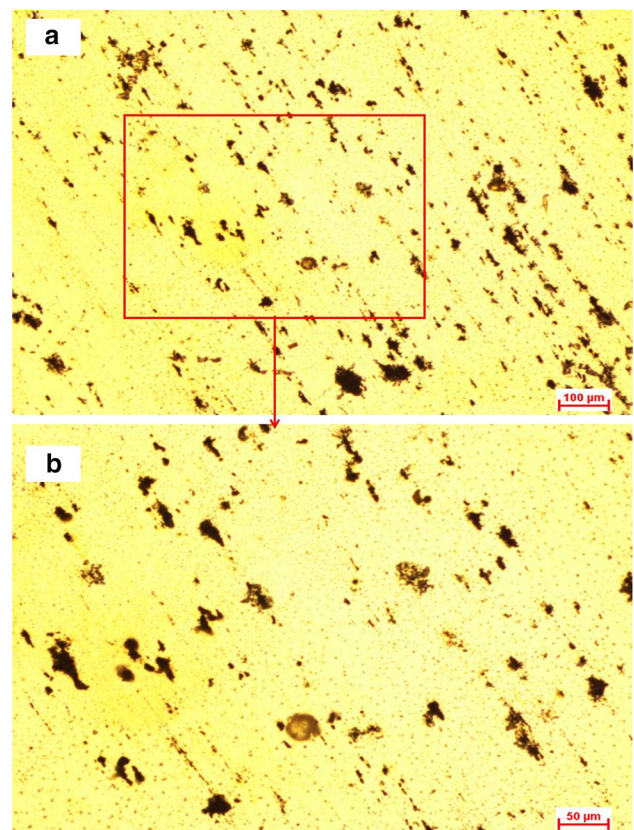


**Fig. 5** Optical photomicrographs of the as-received AA2519-T8 aluminum alloy at different magnifications showing morphology and distribution of second phase particles

micrographs confirming the alignment of the second phase particles along the rolling direction are presented in Fig. 6. The alignment of particles may not be unconnected with the initial cold work applied to the material before artificial

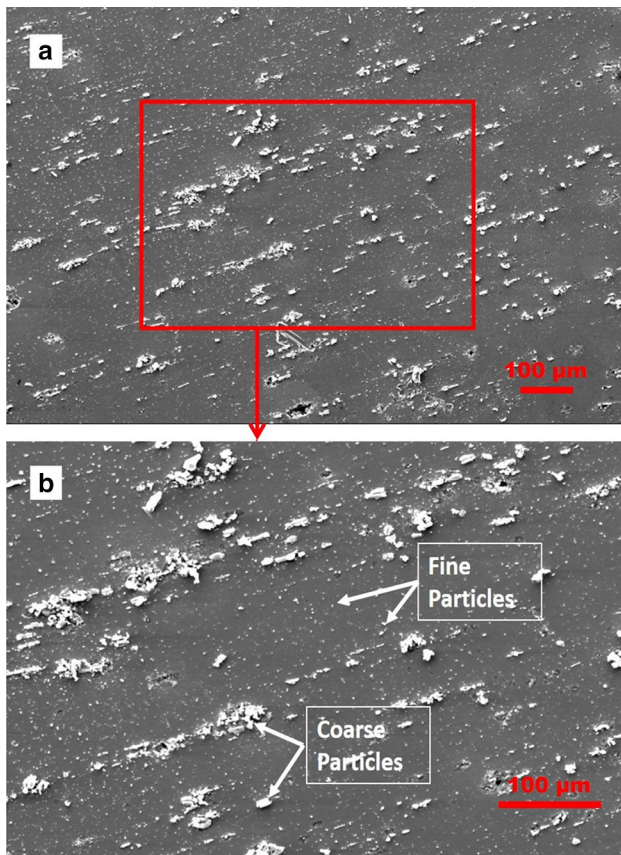


**Fig. 6** SEM photomicrographs of the as-received AA2519-T8 aluminum alloy at different magnifications showing two types of second phase particles

aging. The fine particles, round and irregular in shape, are less than 1  $\mu\text{m}$  in size, and are clearly identified in the SEM micrographs (Fig. 6b) at higher magnification. The shape factor of the fine particles was found to be 0.9. It is also observed that the fine particles have higher density and are more uniformly distributed than the coarse particles.

In Wang and Starink [17], the second phase particles are suggested to be intermetallic phases formed by liquid–solid eutectic reaction during solidification. It was also reported that these phases transform with further heat treatment and that their sizes range from one to tens of micrometers. The variation in size of these particles can be attributed to nature of different intermetallic phases in various aluminum alloys and other factors like solidification rate, impurity content and rate of deformation during mechanical and thermo-mechanical processing. These second phases may be classified into insoluble and soluble phases based on their stability during heat treatment. Wang and Starink [17] indicated that the insoluble phases arise as a result of the presence of impurity atoms of Fe and Si which have low solubility in aluminum that is alloyed with Mg, while the other phase is soluble as long as the alloying elements are kept below

solubility limits. In the same study, with the help of back-scatter electron images and element mappings, the researchers found structures of some as-cast Al–Cu–Mg alloys to be a mixture of constituents which include  $\text{Al}_7\text{Cu}_2\text{Fe}$ ,  $\text{Al}_{12}\text{Fe}_3\text{Si}$ ,  $\text{Al}_6(\text{Fe,Cu})$ , and soluble particles of  $\text{Al}_2\text{Cu}$ ,  $\text{Al}_2\text{CuMg}$ , and  $\text{Mg}_2\text{Si}$ . Other dispersoid-forming elements in the composition (Table 1) of the aluminum alloy in the current investigation are Mn and Zr. The complex addition of dispersoid-forming elements was reported to enhance significant resistance to recrystallization [27].

While second phase particles are widely believed to have adverse effects on mechanical properties, due to their contribution to crack initiation, crack growth and corrosion, the main strengtheners heat-treatable Al–Cu alloys to which AA2519 belongs are semi-coherent and coherent particles of  $\theta''$ -( $\text{Al}_2\text{Cu}$ ) and  $\theta'$ -( $\text{Al}_2\text{Cu}$ ) phases respectively [28].  $\theta''$  and  $\theta'$  phase precipitates are phases that form during precipitation heat treatment of Al–Cu alloys and they are produced from the transformation of Guinier Preston (GP) zones; clusters of solute atoms resulting from the decomposition of the supersaturated solid solution (SSS) obtained after solution heat treatment. The suggested precipitation sequence for the Al–Cu–Mg alloys is  $\text{SSS} \rightarrow \text{GPB zones} \rightarrow \text{S}'' \rightarrow \text{S}' \rightarrow \text{S}(\text{Al}_2\text{CuMg})$ . Therefore, the major strengthening precipitates suggested for this alloy are  $\theta'$ ( $\text{Al}_2\text{Cu}$ ) and  $\text{S}'(\text{Al}_2\text{CuMg})$  phases. They are coherent particles which are very effective in pinning down dislocation and improve strength. These precipitates, which are formed during age-hardening, are normally demonstrated on transmission electron microscope by selected area diffraction pattern as thin plates with thickness of a few nanometers [7, 29]. In addition to 5.3–6.4 wt% Cu, the Al–Cu–Mg alloy contains Mg (0.05–0.4 wt%) with Cu/Mg ratio  $\geq 15$  [21, 30]. This composition modification has been reported to be responsible for the increase in strength through the formation of second phase particles [10].

### Microstructure Evolution During Dynamic Loading at High Strain Rates

When the aluminum alloy was deformed at strain rates of  $3000 \text{ s}^{-1}$  and below, the optical microstructure did not indicate any change in microstructure compared to that of the as-received alloy. The deformation was heterogeneous as there is no evidence of strain localization in the microstructure. Figure 7 shows the optical micrograph of a specimen deformed at  $3500 \text{ s}^{-1}$ . The figure shows a circular shape ASB containing a much lower density of second phase particles in comparison with other regions in the microstructure. The circular shear band is concentric with the circular cross-section of the impacted plane of the specimen. Circular shaped ASBs have also been observed on the impacted plane of other metallic alloys [31]. The

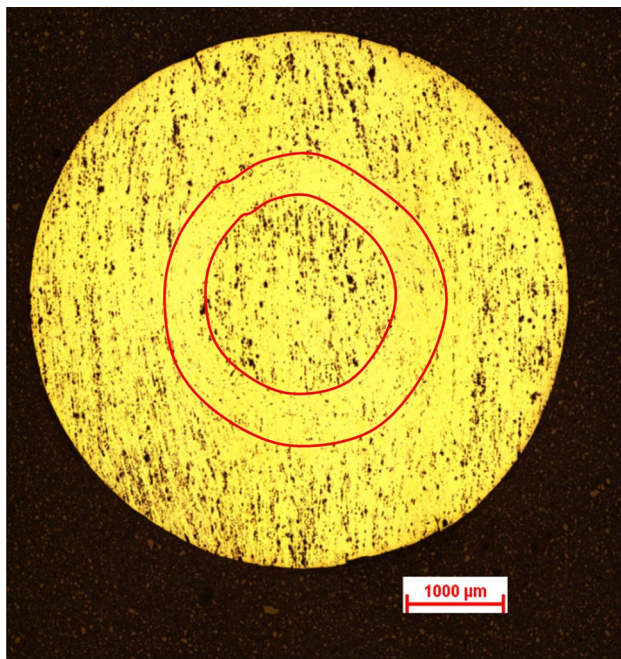


**Fig. 7** Optical photomicrograph showing ASB that formed in a specimen deformed at a strain rate of  $3500 \text{ s}^{-1}$

presence of the ASBs is an indication of heterogeneous deformation in the alloy when deformed at a strain rate of  $3500 \text{ s}^{-1}$  and above. This is usually as a result of the significant amount of thermal softening, occurring as a result of the transient adiabatic heating in the local region of the shear bands during large plastic deformation. The beginning of the evolution of ASB is often marked by a point of thermal instability that is reached when thermal softening eventually becomes larger than the rate of strain hardening lead to sharp drop in stress in stress–strain curves. In reality, this thermal instability is not perfectly adiabatic. Some of the heat generated by plastic flow is always conducted away from the deforming zone which may or may not be significant depending on the thermal diffusivity of the target material [13]. The phenomenon has been referred to as ‘catastrophic’ thermoplastic shear by Rogers [32] and Bai et al. [33] to indicate that ASB usually leads to fracture.

The second phase particles were observed to have dissolved partially into the matrix within the shear band. SEM micrograph showing only fine particles inside the shear band is presented in Fig. 8. The mean size of the undissolved particles within the shear band was determined to be  $11 \pm 3 \mu\text{m}$  with a shape factor of 0.9. Micrographs showing the morphology of these coarse constituent particles outside the ASB are presented in Fig. 9. The coarse particles outside the ASB are  $40 \pm 9 \mu\text{m}$  in size but with a slight difference in shape factor of 0.8 when compared to the as-received alloy. Apparently, the small change in shape factor may be due to their fractured, strained or partially dissolved nature

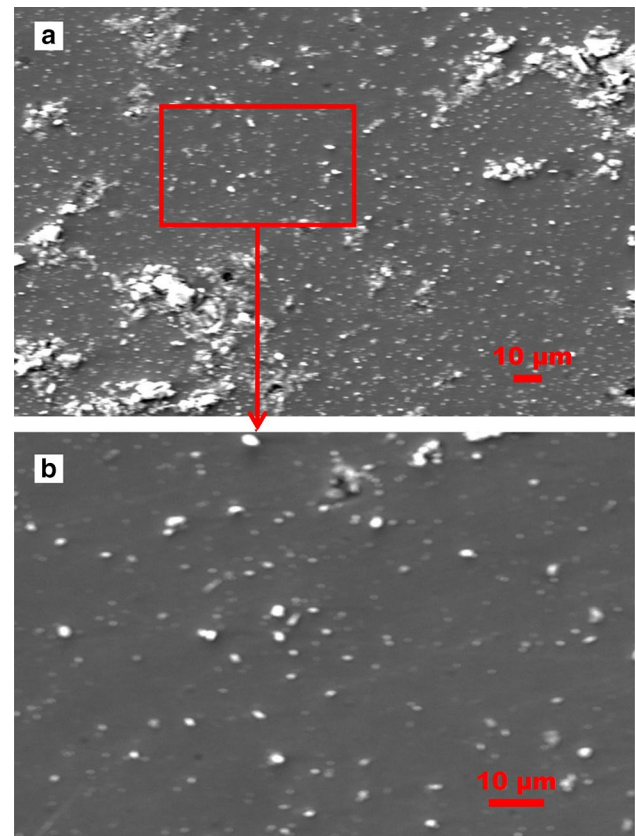


**Fig. 8** SEM photomicrographs of the deformed specimen (at  $3500 \text{ s}^{-1}$ ), showing region of adiabatic shear band and morphology and distribution of second phase particles in this region

after deformation. Fracture of second phase particles can be observed in the microstructures presented in Fig. 9.

## Conclusion

The plastic deformation of cylindrical specimens of AA2519-T8 aluminum alloy with an aspect ratio of 1 was investigated at high strain rates in compression. It was determined that the SRS coefficient of the alloy is 0.0486 at 0.12 plastic strain. Peak flow stress of 560 MPa was obtained when the alloy was deformed at a strain rate of  $3500 \text{ s}^{-1}$ . The peak flow stress decreased as the strain rate was reduced. The microstructure of the deformed specimen exhibited an evolving circular ASB on the compression plane of the specimen. The evolving ASB comprised partially dissolved and fractured second phase particles. The regions surrounding the shear bands showed little or no change in the size of particles. However, the coarse constituent particles were observed as an agglomeration of fractured pieces, thus having a shape factor that is different from that of the second particles contained in the as-received alloy.

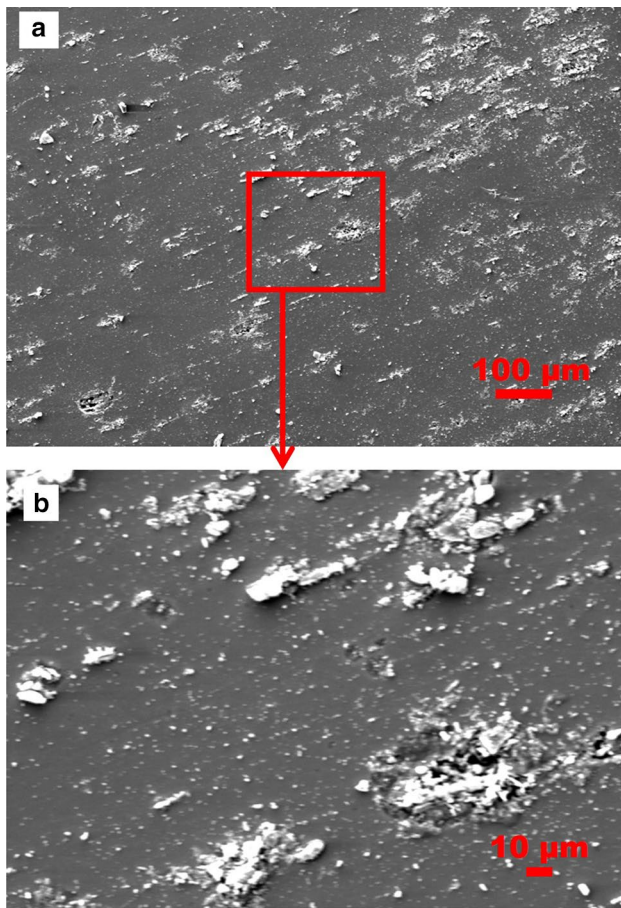


**Fig. 9** SEM photomicrographs showing the morphology and distribution of the second phase particles outside the ASB region in the specimen deformed at  $3500 \text{ s}^{-1}$

**Acknowledgements** The authors would like to acknowledge the financial support from the Department of Defense through the research and educational program HBCU/MSI (contract # W911NF-15-1-0457) under the direct supervision of Dr. Joycelyn S. Harrison (Program Manager, AFOSR Complex Materials and Devices Program) and Patricia Huff (HBCU/MI Program Manager, Army Research Office).

## References

- Campbell FC (2006) Manufacturing technology for aerospace structural materials, 1st edn. Elsevier, San Diego
- Warmuzek M (2004) Metallography and microstructures. In: Voort GFV (ed) ASM handbook, vol 9. ASM International, Materials Park, pp 711–751
- The Aluminum Association Inc (2006) International alloy designations and chemical composition limits for wrought aluminum and wrought aluminum alloy. The Aluminum Association Inc, Arlington
- Immarigeon JP, Holt RT, Koul AK, Zhao L, Wallace W, Beddoes JC (1995) Lightweight materials for aircraft applications. *Mater Charact* 35(1):41–67
- United States Department of Defense (2004) Department of defense handbook: metallic materials and elements for aerospace vehicle structures, United States Department of Defense, Ohio
- Sokkalingam R, Venkatesan K, Sabari SS, Malarvizhi S, Balasubramanian V (2014) Effect of post-weld aging treatment on tensile properties of gtaw welded armor grade AA2519-T87 aluminum alloy joints. *Int J Res Sci Eng* 3(11):316–320
- Zuiko I, Gazizov M, Kaibyshev R (2016) Superplasticity of an AA2519 aluminum alloy. *Mater Sci Forum* 278–284, 838–839
- (Rusty) Gray GT III (2000) Classic split-Hopkinson pressure bar testing. In: Kuhn H, Medlin D (eds) ASM handbook, vol 8. ASM International, Materials Park, pp 427–430
- GT (Rusty) Gray (2012) High strain-rate deformation: mechanical behavior and deformation substructures induced. *Annu Rev Mater Res* 42(1):285–303
- Embury JD, Lloyd DJ, Ramachandran TR (1989) Strengthening mechanisms in aluminum alloys. In: Aluminum alloys - contemporary research and applications, vol 31. Elsevier, Burlington, pp 579–601
- Aernoudt E, Houtte PV, Leffers T (1996) Deformation and textures of metals at large strain. In: Mughrabi H (ed) Plastic deformation and fracture of materials, vol 6. Wiley, Weinheim, pp 90–133
- Wright TW (2012) Theory of adiabatic shear bands. In: Adiabatic shear localization, 2nd edn. Elsevier, Oxford, pp 215–246
- Dodd B, Bai Y (2012) Introduction to adiabatic shear localization. In: Adiabatic shear localization. Elsevier, Waltham, pp 1–20
- Hodowany J, Ravichandran G, Rosakis AJ, Rosakis P (2000) Partition of plastic work into heat and stored energy in metals. *Exp Mech* 40(2):113–123
- Odeshi AG, Adesola AO, Badmos AY (2013) Failure of AA6061 and 2099 aluminum alloys under dynamic shock loading. *Eng Fail Anal* 35:302–314
- Perez-Bergquist SJ, (Rusty) Gray GTR, Cerreta EK, Trujillo CP, Perez-Bergquist A (2011) The dynamic and quasi-static mechanical response of three aluminum armor alloys: 5059, 5083 and 7039. *Mater Sci Eng A* 528(29–30):8733–8741
- Wang SC, Starink MJ (2005) Precipitates and intermetallic phases in precipitation hardening Al–Cu–Mg–(Li) based alloys. *Int Mater Rev* 50(4):193–215
- Ramesh K (2008) High rates and impact experiments. In: Sharpe WJ (ed) Springer handbook of experimental solid mechanics. Springer, New York, pp 929–959
- Song Y, Guan Z, Li Z, Wang M (2007) Theoretical and metrical standardization of strain rate sensitivity index. *Sci China Ser E: Technol Sci* 50(6):714–735
- Macar M (2014) Investigation of dynamic behavior of aluminum alloy armor materials. Ph.D. Dissertation, Ankara
- Gao Z, Zhang X, Chen MA (2008) Influence of strain rate on the precipitate microstructure in impacted aluminum alloy. *Scripta Mater* 59(9):983–986
- Cadoni E, Dotta M, Forni D, Kaufmann H (2017) Tensile behaviour of commercial aluminum alloys used in armor applications at high strain rate. *Proc Eng* 197:168–175
- Prabu SB, Padmanabhan KA (2014) Superplasticity in and superplastic forming of aluminum-lithium alloys. In: Prasad NE, Gokhale AA, Wanhill RJH (eds) Aluminum–lithium alloys: processing, properties and applications. Elsevier, Oxford
- Armstrong RW, Walley SM (2008) High strain rate properties of metals and alloys. *Int Mater Rev* 53(3):105–128
- Wei Q (2007) Strain rate effects in the ultrafine grain and nanocrystalline regimes - influence on some constitutive responses. *J Mater Sci* 42(5):1709–1727
- Thom M (2017) The elastic-plastic response of aluminum alloys under multiaxial fatigue loading. M.Sc. Thesis, Department of Mechanical Engineering, Howard University, Washington

27. Tsivoulas D, Prangnell PB (2014) The effect of Mn and Zr dispersoid-forming additions on recrystallization resistance in Al–Cu–Li AA2198 sheet. *Acta Mater* 77:1–16
28. Zuiko IS, Gazizov MR, Kaibyshev RO (2016) Effect of thermo-mechanical treatment on the microstructure, phase composition, and mechanical properties of Al–Cu–Mn–Mg–Zr alloy. *Phys Met Metall* 117(9):906–919
29. Xiao-peng L, Hui-Zhong LI, Lan H, Tao H, Bing MA, Yong LIU (2012) Microstructural evolution of 2519-T87 aluminum alloy obliquely impacted by projectile with velocity of 816 m/s. *Trans Non-ferrous Met Soc China* 22(6):1270–1279
30. Cayless RBC (1990) Alloy and temper designation systems for aluminum and aluminum alloys. In: *ASM handbook*. ASM International, Materials Park, pp 39–144
31. Odeshi AG, Bassim MN, Al-meeri S (2009) High strain-rate fracture and failure of a high strength low alloy steel in compression. *Mater Sci Eng A* 525(1–2):96–101
32. Rogers HC (1979) Adiabatic plastic deformation. *Annu Rev Mater Sci* 9:283–311
33. Bai Y, Cheng C, Yu S (1986) On the evolution of thermoplastic shear band. *Acta Mech Sin* 2:1–7